iScience

CellPress
OPEN ACCESS

Article

Gate-tunable circular phonon dichroism effect in bilayer graphene

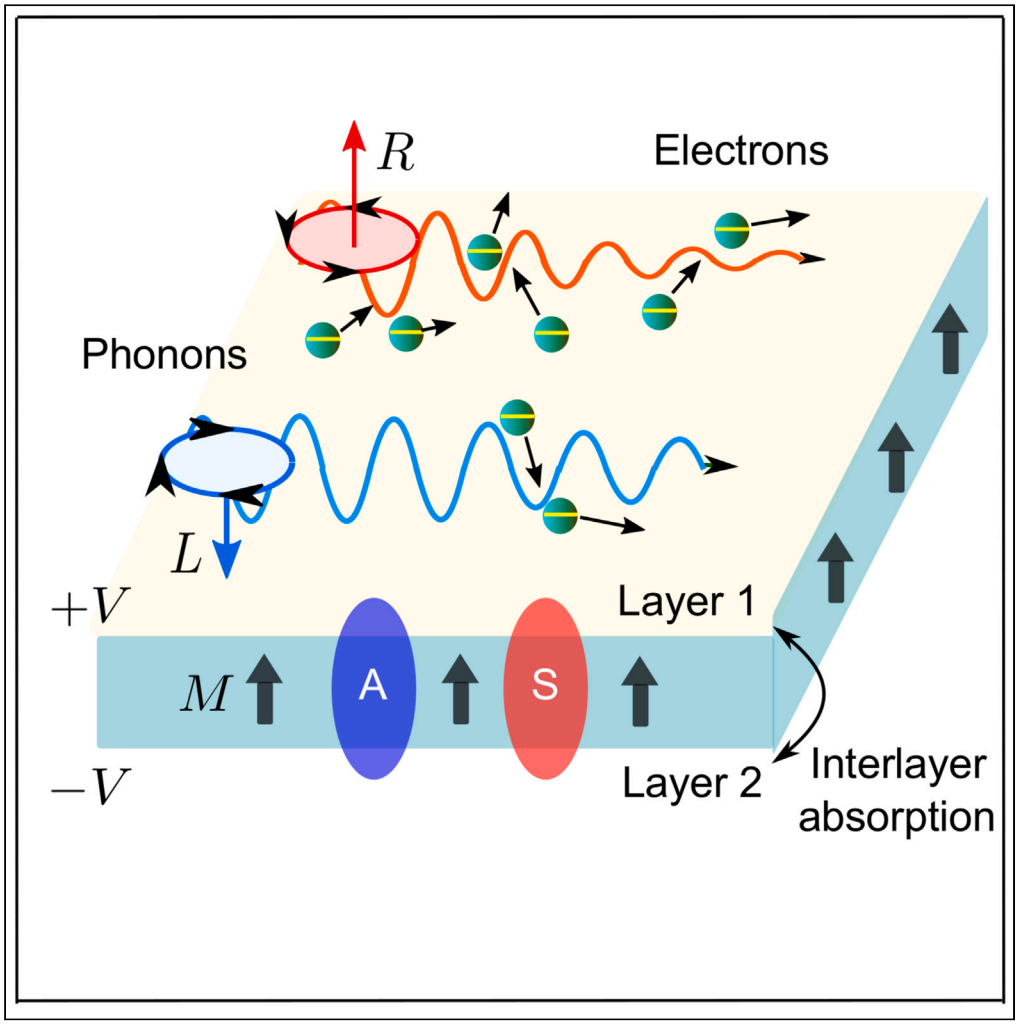

Wen-Yu Shan

wyshan@gzhu.edu.cn

Highlights

Circular phonon dichroism effect in magnetic bilayer graphene is given

Gate tunability of circular phonon dichroism is explored

Layer-symmetric and layer-antisymmetric channels of phonon absorption are predicted

Interlayer phonon absorption by electrons is predicted

Shan, iScience 27, 109374
April 19, 2024
https://doi.org/10.1016/j.isci.2024.109374

iScience

CellPress
OPEN ACCESS

Article

Gate-tunable circular phonon dichroism effect in bilayer graphene

Wen-Yu Shan[1,2,*]

SUMMARY

Circular phonon dichroism effect has been proposed in two-dimensional materials; however, the lack of tunability hinders the exploration of the effect. Here, we investigate the role of dual-gating-induced inversion symmetry breaking in the circular phonon dichroism effect in bilayer graphene. We find that the introduction of inversion symmetry breaking modifies the response in the layer-symmetric and layer-antisymmetric channels, and results in the occurrence of phonon dichroism in the cross-channel. In the layer representation, the inversion symmetry breaking breaks the equality of intralayer circular phonon dichroism and enhances the interlayer response. Our results suggest that layer degree of freedom provides possibilities to tune phonon dynamics, which paves a way toward different physics and applications of two-dimensional acoustoelectronics and layertronics.

INTRODUCTION

Recent years have witnessed a rapid development of topological or band geometric properties of electronic systems.[1] When more than one type of carriers, such as electrons and phonons, are present in the system, topological or band geometric information of electrons can be transferred to phonons through some specific form of electron-phonon coupling. This could significantly change the phonon physics and give rise to various intriguing properties of phonons, such as giant phonon orbital magnetic moment,[2–9] phonon Hall viscosity,[10] phonon rotoelectric effect,[11] phonon magnetochiral effect,[12,13] phonon helicity,[14,15] phonon dichroism,[16–18] etc.

Circular phonon dichroism (CPD) effect, describing the different absorption between left- and right-handed circularly polarized phonons through the electron-phonon coupling mechanism (see Figure 1), has been discussed in Weyl semimetals[16] and monolayer transition metal dichalcogenides $MoTe_2$.[17–19] To exhibit the effect, time-reversal symmetry breaking is required by applying either magnetic field or external magnetization. Physically, such effect is recognized to originate from nonlocal band geometric quantities of electrons and reduce to pure Fermi-surface properties for acoustic phonons.[18] Despite these early works, experimental progress is relatively slow. Up to now, there are only few works discussing the effect of Landau levels on the phonon dispersion or circular dichroism in graphene,[20–22] such as magnetophonon resonance. By contrast, anomalous CPD without using Landau levels has not been realized yet.[17] One reason may be due to the lack of tunability of the effect in experiments.

On the other hand, bilayer graphene may provide an ideal platform to study the phonon dichroism effect, thanks to the dual-gating technique.[23–27] Such technique allows us to tune the Fermi energy and band gap independently by combining the top and bottom gates (see Figure 2). This technique has been successfully used in the nonlocal transport measurements of bilayer graphene to demonstrate the valley Hall effect.[27,28] Moreover, phonon magnetic moment has recently been discussed in bilayer graphene by first-principles calculations,[7] which shows high tunability by changing the gate voltage. The results also show significant deviation from the classical theory, which highlight the importance of taking into account topology or band geometry of electrons when evaluating the phonon magnetic moment. Given that the CPD effect is also related to band geometric quantities,[18] it motivates us to investigate the possibility of gate-tunable phonon dichroism in bilayer graphene. This also provides an opportunity to introduce the layer degree of freedom in the CPD effect as the layer Hall effect in bilayer topological antiferromagnet.[29,30]

In this work, we study the effect of dual-gating-induced inversion symmetry breaking on the CPD effect in bilayer graphene. We find that in the absence of inversion symmetry breaking, the CPD exists in the layer-symmetric (*S*) and -antisymmetric (*A*) channels, whereas it vanishes in the cross-channel. The introduction of layer potential difference breaks the inversion symmetry, thus modifies the layer-*S* and layer-*A* CPD, and induces the CPD in the cross-channel. In the layer representation, such difference breaks the equality of intralayer CPD from different layers, and enhances the interlayer CPD. Our results suggest that layer degree of freedom provides possibilities to tune phonon dynamics through electron-phonon coupling in bilayer systems. This paves the way toward different physics and applications of two-dimensional acoustoelectronics and layertronics.

[1]Department of Physics, School of Physics and Materials Science, Guangzhou University, Guangzhou 510006, China
[2]Lead contact
*Correspondence: wyshan@gzhu.edu.cn
https://doi.org/10.1016/j.isci.2024.109374

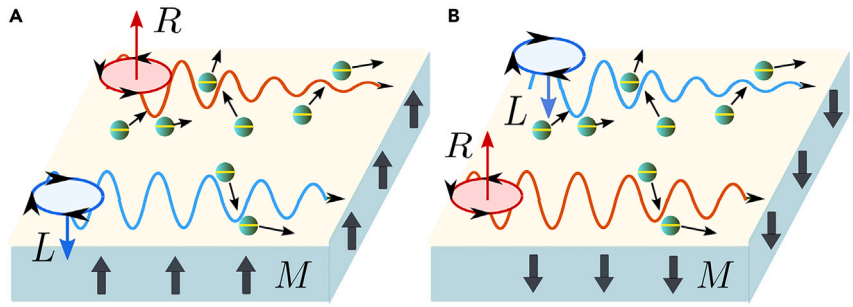

Figure 1. Schematics of circular phonon dichroism (CPD)

(A) CPD with external magnetization M. R and L label right-handed and left-handed circularly polarized phonons, respectively. More (Less) scatterings by electrons imply greater (smaller) absorption of phonons.

(B) CPD with external magnetization $-M$.

RESULTS

Model

We start with the low-energy effective model of electrons for Bernal-stacked bilayer graphene in the vicinity of valley $\pm K$[31–33]

$$H_e(\boldsymbol{k}) = t_0(\eta k_x\sigma_x + k_y\sigma_y)s_0\tau_0 - \frac{t_{ab}}{2}(\sigma_x\tau_x + \sigma_y\tau_y)s_0 + \frac{\lambda_R}{2}(\eta\sigma_x s_y - \sigma_y s_x)\tau_0 + M\sigma_0 s_z\tau_0 + V\sigma_0 s_0\tau_z, \quad \text{(Equation 1)}$$

where $\eta = \pm 1$ labels valley $\pm K$ degree of freedom. $\boldsymbol{\sigma}$, $\boldsymbol{s}$, and $\boldsymbol{\tau}$ are Pauli matrices acting on sublattice (A/B), spin ($\uparrow/\downarrow$), and layer ($l = 1,2$) subspaces, respectively. The first term with $t_0 = \hbar v$ describes the nearest-neighbor hopping within each layer. The second term is the interlayer hopping between sublattice A in layer 2 and B in layer 1 (see Figure 2). These two terms constitute the model for pristine bilayer graphene. By depositing bilayer graphene on magnetic substrates, such as ferromagnetic insulator yttrium iron garnet (YIG),[34,35] Rashba spin-orbit coupling (SOC) and exchange interaction are introduced, corresponding to the third and fourth term. The fifth term represents the potential energy difference in the two layers induced by perpendicular electric field. Here we use the values quoted in the study by Mariani et al.[36]: $t_0 = 5.26$ eV $\cdot$Å and $t_{ab} = 0.39$ eV. Intrinsic SOC is weak in bilayer graphene with YIG substrate, and it can be neglected in our discussion.

The form of electron-phonon coupling H_{e-ph} for bilayer graphene can be derived by considering local variations of areas or modifications of bond lengths between neighboring atoms.[36–38] The former mechanism results in scalar (labeled by sc) deformation potentials within each layer, which can be decomposed into symmetric (labeled by S) and antisymmetric (labeled by A) deformations between the two layers (see Figure 3). That is, $H^{sc}_{e-ph} = H^{sc}_{e-ph,S} + H^{sc}_{e-ph,A}$, where $H^{sc}_{e-ph,S/A} = \boldsymbol{u}_{S/A}(\boldsymbol{q})\cdot\widehat{T}^{sc}_{S/A}(\boldsymbol{q})$ and

$$\widehat{T}^{sc}_S(\boldsymbol{q}) = \boldsymbol{q}\sigma_0\tau_0 s_0, \quad \widehat{T}^{sc}_A(\boldsymbol{q}) = -\boldsymbol{q}\sigma_0\tau_z s_0. \quad \text{(Equation 2)}$$

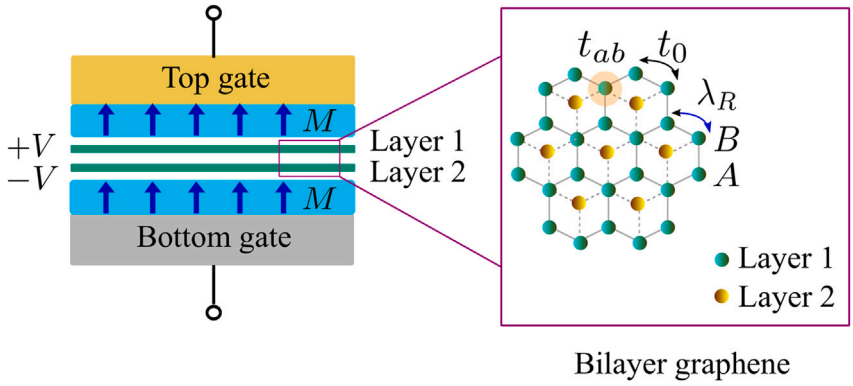

Figure 2. Schematics of dual-gated Bernal-stacked bilayer graphene

M is the external magnetization due to magnetic substrates. $\pm V$ is the potential energy induced by dual gate. t_0 and t_{ab} denote intralayer nearest-neighbor hopping and interlayer hopping, respectively. λ_R denotes the Rashba spin-orbit coupling.

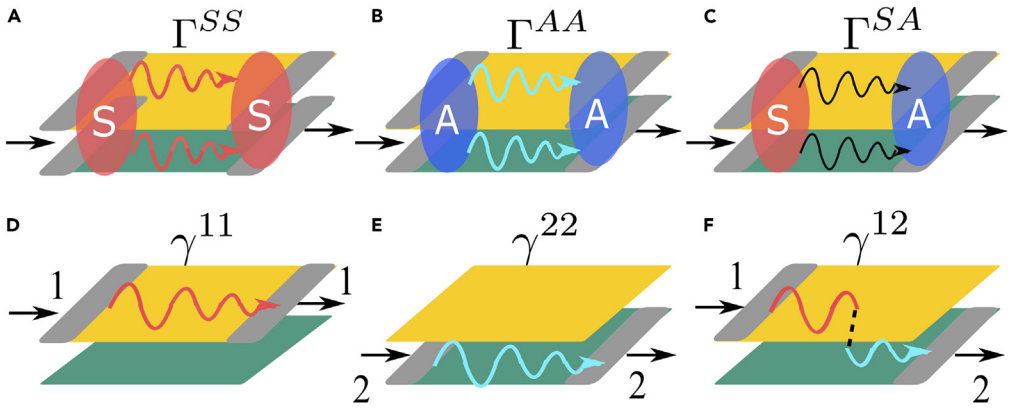

Figure 3. Schematics of phonon injection and absorption of bilayer graphene

(A–C) In the layer-symmetric (*S*) and -antisymmetric (*A*) representation. Γ are the phonon absorption coefficients in the representation.

(D–F) In the layer 1 (2) representation. γ are the phonon absorption coefficients in the representation.

Symmetric (antisymmetric) deformations $\boldsymbol{u}_{S/A}(\boldsymbol{q})$ are introduced by combining the deformations from each layer as follows:

$$\boldsymbol{u}_{S/A}(\boldsymbol{q}) = \frac{\boldsymbol{u}^{(2)}(\boldsymbol{q}) \pm \boldsymbol{u}^{(1)}(\boldsymbol{q})}{2}, \quad \text{(Equation 3)}$$

where $\boldsymbol{u}^{(l)}(\boldsymbol{q})$ ($l = 1,2$) is the Fourier transformation of real-space in-plane deformation $\boldsymbol{u}^{(l)}(\boldsymbol{r})$ of atoms *A* or *B* within layer *l*. Since we are only interested in the acoustic phonon modes, *A* and *B* atoms in the same layer share the same deformation. Moreover, as phonon dichroism is

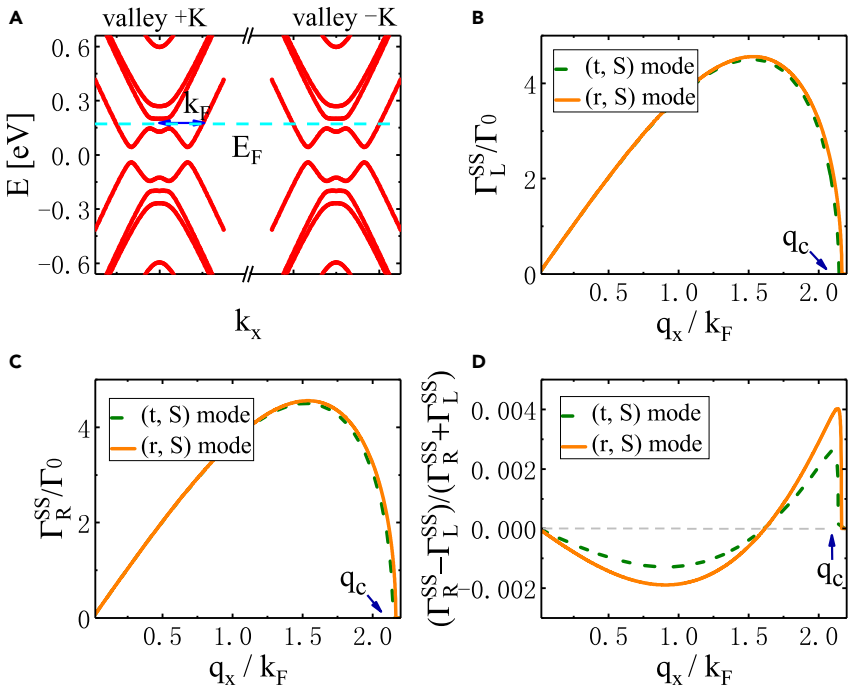

Figure 4. Phonon absorption coefficients in the layer-*S* channel of bilayer graphene without layer potential difference

(A) Electronic band structure of Bernal-stacked bilayer graphene without layer potential difference *V*. E_F is the Fermi energy and k_F is the Fermi wave vector at valley $+K$.

(B–D) The layer-*S* absorption coefficients of left-handed, right-handed circularly polarized symmetric phonons Γ_L^{SS}, Γ_R^{SS} and their differences (in units of Γ_0), respectively. Orange solid (green dashed) curve labels longitudinal (transverse) layer-symmetric phonon modes. q_c is the critical phonon wave vector. Parameters: t_0 = 5.26 eV ·Å, t_{ab} = 0.39 eV,[36] λ_R = 0.1 eV, *M* = 0.2 eV, *V* = 0, E_F = 0.18 eV, k_F = 0.1 Å^{-1}, *g* = 1.5 eV,[37] $\Gamma_0 = 3.86\times10^8$ s^{-1}. Sound velocity $v_r = 2.06\times10^4$ m/s, $v_t = 1.37\times10^4$ m/s.[36]

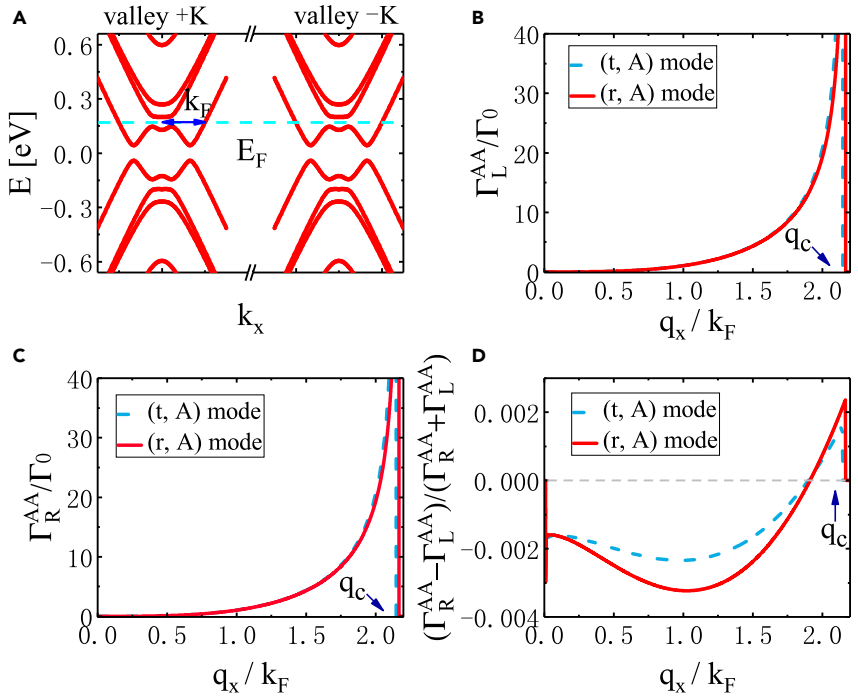

Figure 5. Phonon absorption coefficients in the layer-*A* channel of bilayer graphene without layer potential difference

(A) Electronic band structure of Bernal-stacked bilayer graphene without layer potential difference V, which is identical to Figure 4A. E_F is the Fermi energy and k_F is the Fermi wave vector at valley $+K$.

(B–D) The layer-A absorption coefficients of left-handed, right-handed circularly polarized symmetric phonons Γ_L^{AA}, Γ_R^{AA} and their differences (in units of Γ_0), respectively. Red solid (blue dashed) curve labels longitudinal (transverse) layer-antisymmetric phonon modes. The parameters are the same as those adopted in Figure 4.

only related to the absorption of in-plane components of phonon modes, we neglect the out-of-plane (flexural) components of phonons in the calculation. $\hat{T}^{sc}_{S/A}(\boldsymbol{q})$ can be regarded as effective force acting on nuclei by electrons through the scalar-type electron-phonon coupling. For scalar deformation potentials, $\hat{T}^{sc}_{S/A}(\boldsymbol{q})$ is valley independent and has the same form for both valley K and $-K$. In contrast to the symmetric deformation $H^{sc}_{e-ph,S}$, there is an additional layer index τ_z for antisymmetric deformation $H^{sc}_{e-ph,A}$.

On the other hand, the mechanism with neighboring bond-length changes modifies the hopping energies, and also the Hamiltonian $H_e(\boldsymbol{k})$. For Dirac-type Hamiltonian $H_e(\boldsymbol{k})$, such modification behaves as pseudo-gauge potentials (labeled by ps).[36–40] Similar to the scalar deformation potentials, pseudo-gauge potentials can be decomposed into symmetric and antisymmetric channels between the two layers: $H^{ps}_{e-ph} = H^{ps}_{e-ph,S} + H^{ps}_{e-ph,A}$, where $H^{ps}_{e-ph,S/A} = u_{S/A}(\boldsymbol{q})\cdot\hat{T}^{ps}_{S/A}(\boldsymbol{q})$. For valley K ($\eta = 1$), the effective force operators read

$$\hat{T}^{ps,\eta=1}_{A}(\boldsymbol{q}) = -\hat{T}^{ps,\eta=1}_{S}(\boldsymbol{q})\tau_z = -[\boldsymbol{q}\cdot\boldsymbol{\sigma}^*, (\boldsymbol{q}\times\boldsymbol{\sigma}^*)_z]\tau_z s_0. \quad \text{(Equation 4)}$$

For valley $-K$ ($\eta = -1$), they can be related to valley K by $\hat{T}^{ps,\eta=-1}_{S/A}(\boldsymbol{q}) = \mathcal{K}[\hat{T}^{ps,\eta=1}_{S/A}(\boldsymbol{q})]$, where $\mathcal{K}$ is the complex conjugation operator. The valley-dependent forms of pseudo-gauge fields are a result of time-reversal symmetry of the system in the absence of magnetization. The pseudo-gauge potentials in the symmetric channel share the same form as that in monolayer transition metal dichalcogenides,[17] whereas for the antisymmetric channel, there is an additional layer index τ_z.

To study the phonon dichroism, we also need to consider the phonon dispersions in bilayer graphene. Following the standard Euler-Lagrange equations at harmonic level,[41] the dispersions of symmetric and antisymmetric in-plane phonon modes are given by[36]

$$\begin{aligned} \omega_{r,S,q} &= \hbar v_r q, \quad \omega_{r,A,q} = \hbar\sqrt{v_r^2 q^2 + 2\Omega_{in}^2}, \\ \omega_{t,S,q} &= \hbar v_t q, \quad \omega_{t,A,q} = \hbar\sqrt{v_t^2 q^2 + 2\Omega_{in}^2}, \end{aligned} \quad \text{(Equation 5)}$$

where r (t) labels the longitudinal (transverse) acoustic phonon mode. $v_r = \sqrt{(2\mu+\lambda)/\rho_0}$ and $v_t = \sqrt{\mu/\rho_0}$ are the sound velocities of longitudinal and transverse phonons, respectively. ρ_0 is the mass density in each layer and μ and λ are the Lam e' coefficients for in-plane stretching. Ω_{in} is the frequency corresponding to the sliding of one layer with respect to the other. For bilayer graphene, parameters are adopted[36]: $\rho_0 = 7.6\times10^{-7}$ kg $\cdot$ m^{-2}, $\mu = 9$ eV $\cdot$ Å^{-2}, $\lambda = 2.25$ eV $\cdot$ Å^{-2}, and $\Omega_{in} = 5\times10^{12}$ Hz. As a result, the sound velocity $v_r = 2.06\times10^4$ m/s and $v_t = 1.37\times10^4$ m/s, which are much smaller than the Fermi velocity of electrons $v = 7.98\times10^5$ m/s. Note that the symmetric phonon modes are gapless at

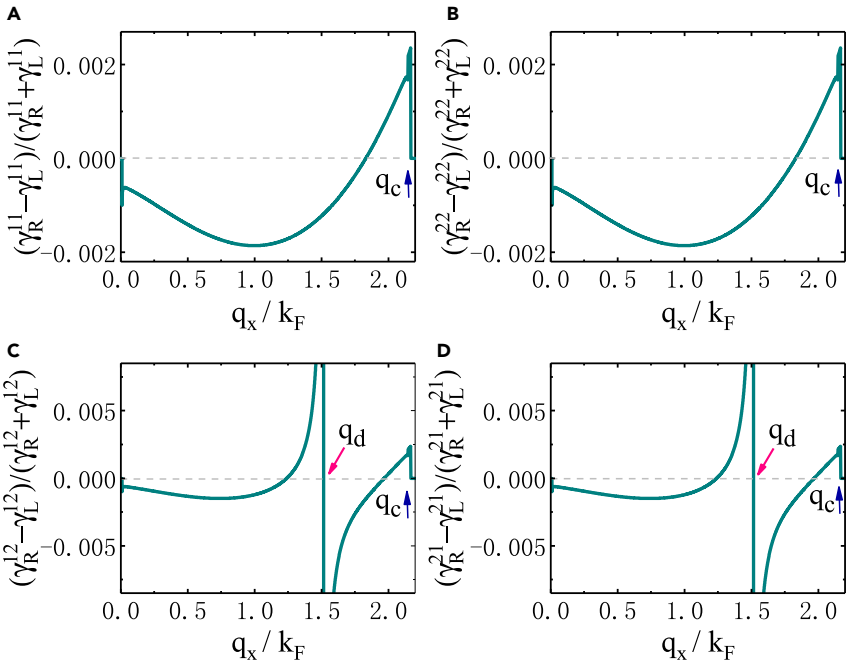

Figure 6. Intralayer and interlayer CPD of bilayer graphene without layer potential difference

(A and B) Intralayer CPD. The contributions from layer-symmetric and layer-antisymmetric phonon modes are included. The parameters are the same as those adopted in Figure 4.

(C and D) Interlayer CPD. The setups of (A–C) correspond to Figures 3D–3F, respectively.

$\boldsymbol{q} = 0$, whereas the antisymmetric phonon modes acquire a small gap $\sqrt{2}\hbar\Omega_{in} = 4.65$ meV at $\boldsymbol{q} = 0$. The effect of the small excitation gap on phonon dichroism will be discussed later.

When phonons are propagating in bilayer graphene, their dynamics are affected by the electron-phonon coupling. In the layer representation with the basis $\{|1,x\rangle,|1,y\rangle,|2,x\rangle,|2,y\rangle\}$, the phonon absorption is characterized by

$$\gamma(\boldsymbol{q},\omega) = \begin{bmatrix} \gamma^{11}(\boldsymbol{q},\omega) & \gamma^{12}(\boldsymbol{q},\omega) \\ \gamma^{21}(\boldsymbol{q},\omega) & \gamma^{22}(\boldsymbol{q},\omega) \end{bmatrix}, \quad \text{(Equation 6)}$$

where the block matrices take the form

$$\gamma^{ll}(\boldsymbol{q},\omega) = \begin{bmatrix} \gamma_D^{ll}+\gamma_{\overline{D}}^{ll} & \gamma_{\overline{E}}^{ll}+i\gamma_E^{ll} \\ \gamma_{\overline{E}}^{ll}-i\gamma_E^{ll} & \gamma_D^{ll}-\gamma_{\overline{D}}^{ll} \end{bmatrix}, ll = 1,2,$$
$$\gamma^{12}(\boldsymbol{q},\omega) = \begin{bmatrix} \gamma_B^{12} & i\gamma_C^{12} \\ i\gamma_I^{12} & \gamma_J^{12} \end{bmatrix}. \quad \text{(Equation 7)}$$

The block matrices $\gamma^{ll}(\boldsymbol{q},\omega)$ describe the intralayer phonon absorption, whereas $\gamma^{12}(\boldsymbol{q},\omega)$ describes the interlayer phonon absorption (see Figures 3D–3F). $\gamma_D^{ll} = (\gamma_{xx}^{ll}+\gamma_{yy}^{ll})/2$ and $\gamma_{\overline{D}}^{ll} = (\gamma_{xx}^{ll}-\gamma_{yy}^{ll})/2$ refer to the symmetric and antisymmetric intralayer longitudinal absorption. $\gamma_{\overline{E}}^{ll} = \mathrm{Re}[\gamma_{xy}^{ll}]$ and $\gamma_E^{ll} = \mathrm{Im}[\gamma_{xy}^{ll}]$ refer to the symmetric and antisymmetric anomalous Hall absorption. $\gamma_B^{12} = \gamma_{xx}^{12}$ and $\gamma_J^{12} = \gamma_{yy}^{12}$ denote the interlayer longitudinal absorption, whereas $\gamma_C^{12} = -i\gamma_{xy}^{12}$ and $\gamma_I^{12} = -i\gamma_{yx}^{12}$ denote the interlayer Hall absorption. The detailed forms of these absorption coefficients are given in Method Details. For left- (right-) handed circularly polarized phonons within layer $l = 1,2$, the polarization vectors $|1,L/R\rangle = \frac{1}{\sqrt{2}}[1,\pm i,0,0]^T$ and $|2,L/R\rangle = \frac{1}{\sqrt{2}}[0,0,1,\pm i]^T$. This gives rise to the intralayer absorption coefficients $\gamma_{L/R}^{ll} \equiv \langle l,L/R|\gamma(\boldsymbol{q},\omega)|l,L/R\rangle = \gamma_D^{ll} \mp \gamma_E^{ll}$, which means that nonzero γ_E^{ll} characterizes the intralayer CPD. Moreover, we have the interlayer absorption $\gamma_{L/R}^{12} \equiv \langle 1,L/R|\gamma(\boldsymbol{q},\omega)|2,L/R\rangle = [\gamma_B^{12}+\gamma_J^{12} \mp \gamma_C^{12} \pm \gamma_I^{12}]/2$, which means that nonzero $\gamma_C^{12} - \gamma_I^{12}$ defines the interlayer CPD.

In the layer-*S* and -*A* representation with the basis $\{|S,x\rangle,|S,y\rangle,|A,x\rangle,|A,y\rangle\}$, the phonon absorption is characterized by

$$\Gamma(\boldsymbol{q},\omega) = \begin{bmatrix} \Gamma^{SS}(\boldsymbol{q},\omega) & \Gamma^{SA}(\boldsymbol{q},\omega) \\ \Gamma^{AS}(\boldsymbol{q},\omega) & \Gamma^{AA}(\boldsymbol{q},\omega) \end{bmatrix}, \quad \text{(Equation 8)}$$

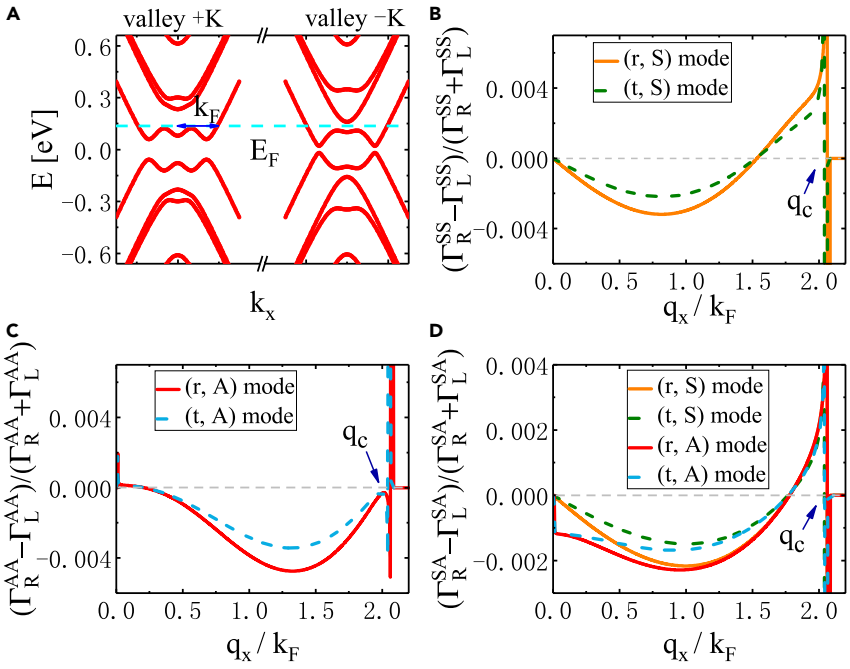

Figure 7. CPD in the layer-*S* and layer-*A* representation of bilayer graphene with layer potential difference

(A) Electronic band structure of Bernal-stacked bilayer graphene with layer potential difference V. E_F is the Fermi energy and k_F is the Fermi wave vector at valley + K. (B–D) CPD of layer-S, layer-A and cross-phonon-responses, which correspond to Figures 3A–3C, respectively. Orange solid (green dashed) curve labels longitudinal (transverse) layer-symmetric phonon modes, red solid (blue dashed) curve labels longitudinal (transverse) layer-antisymmetric phonon modes. Parameters: V = 0.1 eV, E_F = 0.14 eV, k_F = 0.1 Å^{-1}, $\Gamma_0 = 5.79\times10^8$ s^{-1}. Other parameters are the same as those adopted in Figure 4.

where

$$\begin{aligned}\Gamma^{\alpha\alpha}(\boldsymbol{q},\omega) &= \begin{bmatrix}\Gamma_D^{\alpha\alpha}+\Gamma_{\overline{D}}^{\alpha\alpha} & \Gamma_{\overline{E}}^{\alpha\alpha}+i\Gamma_E^{\alpha\alpha}\\ \Gamma_{\overline{E}}^{\alpha\alpha}-i\Gamma_E^{\alpha\alpha} & \Gamma_D^{\alpha\alpha}-\Gamma_{\overline{D}}^{\alpha\alpha}\end{bmatrix},\alpha=S,A,\\ \Gamma^{SA}(\boldsymbol{q},\omega) &= \begin{bmatrix}\Gamma_B^{SA} & i\Gamma_C^{SA}\\ i\Gamma_I^{SA} & \Gamma_J^{SA}\end{bmatrix}.\end{aligned} \qquad \text{(Equation 9)}$$

The block matrices $\Gamma^{SS}(\boldsymbol{q},\omega)$ and $\Gamma^{AA}(\boldsymbol{q},\omega)$ correspond to the phonon absorption in the symmetric and antisymmetric channel, respectively, whereas $\Gamma^{SA}(\boldsymbol{q},\omega)$ corresponds to the phonon absorption in the cross-channel (see Figures 3A–3C). For layer-S or -A left- (right-) handed circular phonons, the polarization vectors $|S,L/R\rangle = \frac{1}{\sqrt{2}}[1,\pm i,0,0]^T$ and $|A,L/R\rangle = \frac{1}{\sqrt{2}}[0,0,1,\pm i]^T$ in the new representation, leading to the absorption coefficients $\Gamma_{L/R}^{\alpha\alpha}\equiv\langle\alpha,L/R|\Gamma(\boldsymbol{q},\omega)|\alpha,L/R\rangle = \Gamma_D^{\alpha\alpha}\mp\Gamma_E^{\alpha\alpha}, \alpha = S,A$. This means that nonzero Γ_E^{SS} (Γ_E^{AA}) defines the layer-S (-A) CPD. For the cross-channel, we find that $\Gamma_{L/R}^{SA}\equiv\langle S,L/R|\Gamma(\boldsymbol{q},\omega)|A,L/R\rangle = \Gamma_B^{SA}+\Gamma_J^{SA}\mp\Gamma_C^{SA}\pm\Gamma_I^{SA}$, which means that nonzero $\Gamma_C^{SA}-\Gamma_I^{SA}$ characterizes the CPD in the cross-channel.

Based on the phonon dynamics theory, one has

$$\begin{aligned}\Gamma_E^{\alpha\alpha}(\boldsymbol{q},\omega) &= \frac{\hbar}{8\pi\rho_0}\sum_{\eta=\pm1}\sum_n\int d^2\boldsymbol{k}\,\mathrm{Im}\left[G_{xy}^{\alpha\alpha,\eta}(\omega,\boldsymbol{k},\boldsymbol{q})\right]_{nn}\\ &\times\delta(E_{\eta,n,\boldsymbol{k}}-E_F)\delta(\omega+E_{\eta,n,\boldsymbol{k}}-E_{\eta,n,\boldsymbol{k}'}),\alpha=S,A,\end{aligned} \qquad \text{(Equation 10)}$$

where $[G_{xy}^{\alpha\alpha,\eta}(\omega,\boldsymbol{k},\boldsymbol{q})]_{nn}$ is a connection between states with wave vector $\boldsymbol{k}$ and $\boldsymbol{k}' = \boldsymbol{k}-\boldsymbol{q}$, triggered by the force operator $\hat{T}_{x/y,\alpha}^{\eta}(\boldsymbol{q})$.[18] $E_{\eta,n,\boldsymbol{k}/\boldsymbol{k}'}$ and $|\psi_{\eta,n,\boldsymbol{k}/\boldsymbol{k}'}\rangle$ are eigen-dispersion and wave functions of $H_e(\boldsymbol{k})$ from Equation 1, respectively. n is the band index and E_F is the Fermi energy. Note that the matrix $\gamma(\boldsymbol{q},\omega)$ and $\Gamma(\boldsymbol{q},\omega)$ from different representations can be related by the transformation

$$\Gamma(\boldsymbol{q},\omega) = 2P^{-1}\gamma(\boldsymbol{q},\omega)P, P = \begin{bmatrix}1&0&-1&0\\0&1&0&-1\\1&0&1&0\\0&1&0&1\end{bmatrix}. \qquad \text{(Equation 11)}$$

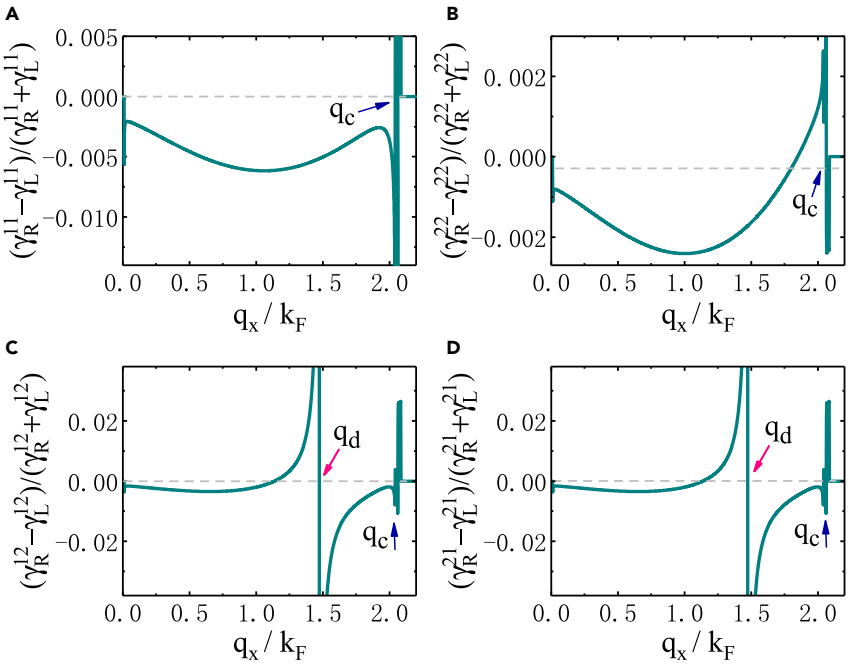

Figure 8. Intralayer and interlayer CPD of bilayer graphene with layer potential difference

(A and B) Intralayer CPD. The contributions from layer-symmetric and layer-antisymmetric phonon modes are included. The parameters are the same as those adopted in Figure 7.

(C and D) Interlayer CPD. The setups of (A–C) correspond to Figures 3D–3F, respectively.

Without layer potential difference

In this section, we show numerical results of CPD of Bernal-stacked bilayer graphene in the absence of layer potential difference, i.e., $V = 0$. When the exchange interaction M is also absent, we find that all types of CPD vanish, in agreement with the requirement of time-reversal symmetry. In this sense, the introduction of M breaks the time-reversal symmetry, which may give rise to the non-vanishing CPD.

The form of electron-phonon coupling is crucial for the occurrence of CPD. For example, when considering the scalar deformation potentials from Equation 2, we find that $\Gamma_E^{SS} = \Gamma_E^{AA} = \Gamma_C^{SA} = \Gamma_I^{SA} = 0$, meaning that the CPD vanishes in the layer-S, layer-A, or cross-channel. Moreover, given the relations between the matrix Γ and γ in Equation 11, we have $\gamma_E^{SS} = \gamma_E^{AA} = \gamma_C^{SA} = \gamma_I^{SA} = 0$, suggesting that CPD is also absent in either intralayer or interlayer channels.

When the pseudo-gauge potentials from Equation 4 are taken into account, we calculate the CPD in the layer-S and layer-A channels, whose results are shown in Figures 4 and 5, respectively. The identical electronic band structure is shown in Figures 4A and 5A. Without loss of generality, we assume that the Fermi level intersects the conduction band and phonons propagate along the x direction. The different absorption coefficients $\Gamma_{L/R}^{SS}$ of left-handed and right-handed circularly polarized phonons in Figures 4B and 4C lead to the layer-S CPD in Figure 4D. As the phonon wave vector q_x increases, we can see that the layer-S CPD shows sign change, then reaches the peak value at the critical point $q_x = q_c$. The critical point q_c is the maximum q_x satisfying the transition condition $\omega + E_{\eta,n,k} = E_{\eta,n,k-q}$ from Equation 10. When q_x becomes larger than q_c, the layer-S CPD vanishes immediately since the phonon-driven intraband electronic transition is prohibited. Orange solid (Green dashed) curve refers to the contribution from the longitudinal (transverse) layer-S phonon modes. These modes share qualitatively similar behaviors since they have the same form of electron-phonon coupling as given by Equation 4.

The results of absorption coefficients Γ^{AA} in the layer-A channel are plotted in Figure 5. Basically, the layer-A CPD in Figure 5D shares qualitatively similar behaviors as the layer-S CPD in Figure 4D. Quantitatively, $\Gamma_{L/R}^{AA}$ is much larger than $\Gamma_{L/R}^{SS}$, despite the fact that the relative differences $(\Gamma_R^{SS/AA} - \Gamma_L^{SS/AA})/(\Gamma_R^{SS/AA} + \Gamma_L^{SS/AA})$ have the same order of magnitude. This suggests that phonon absorption is stronger in the layer-A channel than in the layer-S channel (see Figure 3). Red solid (blue dashed) curve refers to the contribution from the longitudinal (transverse) layer-A phonon modes. Note that there is a difference between the layer-S and layer-A CPD when q_x approaches zero. In Figure 4D, the layer-S CPD vanishes when q_x is close to zero, whereas in Figure 5D, the layer-A CPD shows a sudden jump when q_x approaches zero. Such jump is due to the small excitation gap of layer-A phonon modes in Equation 5.

On the other hand, the absorption coefficients $\Gamma_{L/R}^{SA}$ or $\Gamma_{L/R}^{AS}$ in the cross-channel vanish (see Figure 3). This is because in the absence of layer potential difference V, $\Gamma_{L/R}^{SA} = \gamma_{L/R}^{22} - \gamma_{L/R}^{11} + \gamma_{L/R}^{12} - \gamma_{L/R}^{21} = 0$ as a result of inversion symmetry of bilayer graphene.

Now we analyze the behaviors of CPD in the representation of individual layers. In such representation, the absorption coefficients $\gamma_{L/R}$ can be directly obtained from $\Gamma_{L/R}$ based on the relation (11), whose results are plotted in Figure 6. The setups of Figures 6A–6C correspond to

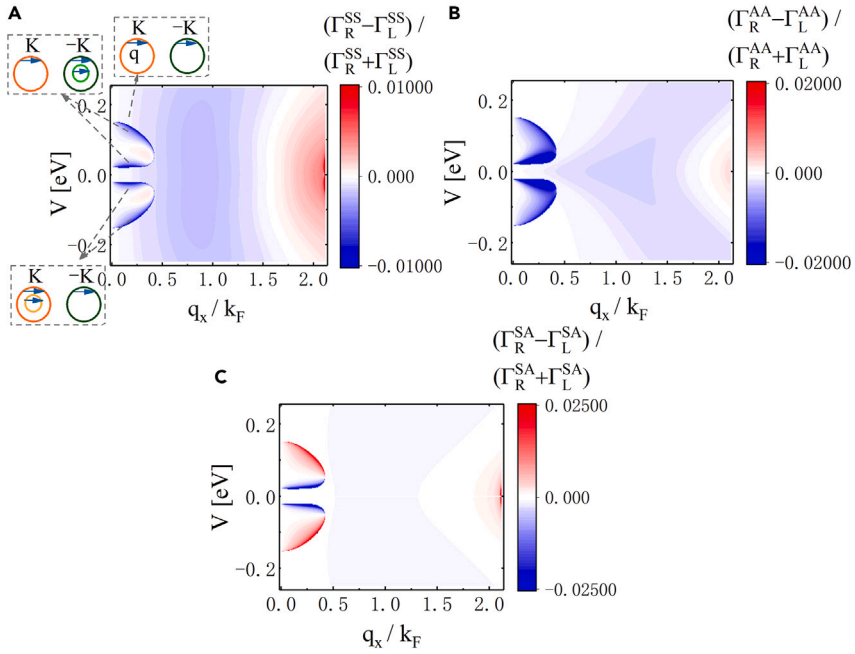

Figure 9. CPD of layer-*S*, layer-*A*, and cross-responses versus phonon wave vector q_x and layer potential difference *V*

(A) CPD of layer-*S* responses. Schematics of Fermi pockets and allowed electronic transitions induced by phonons are shown in the insets. The parameters are the same as those adopted in Figure 4.

(B) CPD of layer-*A* responses.

(C) CPD of cross-responses.

Figures 3D–3F, respectively. Figures 6A and 6B show the intralayer CPD within layer 1 and 2, respectively. Figure 6C shows the interlayer CPD, with the phonon injection in layer 1 and phonon absorption in layer 2. Oppositely, Figure 6D shows the interlayer CPD, with the phonon injection in layer 2 and phonon absorption in layer 1. The contributions from layer-*S* and layer-*A* phonon modes are included. We can see that the behaviors of Figures 6A and 6B are the same, and similarly for Figures 6C and 6D. This can be understood by the fact that in the absence of layer potential difference *V*, bilayer graphene preserves the inversion symmetry and the physical behaviors of the two layers should be identical. The existence of interlayer CPD in Figures 6C and 6D is a result of interlayer coupling of electrons. Note that there is a discontinuous point for interlayer CPD at $q_x = q_d$. This is due to the vanishing absorption coefficients $\gamma_R^{12} + \gamma_L^{12} = \Gamma_D^{SS} - \Gamma_D^{AA}$. In this sense, the discontinuous point q_d can also be found by equalizing the absorption coefficients in the layer-*S* and layer-*A* channels in Figures 4B, 4C, 5B, and 5C.

With layer potential difference

In this section, we show numerical results of CPD in the presence of layer potential difference *V*. The electrical field *E* is proportional to the layer potential difference *V* by the relation $E = (\xi/2d)(V_0 - V)$,[27] where ξ is the dielectric constant, *d* is the thickness of the dielectric layers, and V_0 is the effective offset voltage difference caused by environment-induced carrier doping. The electronic band structure is plotted in Figure 7A, where the Fermi level lies in the conduction band. The band structure with layer potential difference *V* can be directly compared with the energy band under electric field.[25,26] Due to the inversion symmetry breaking induced by the potential difference *V*, band dispersions between valley *K* and $-K$ seem quite different. This leads to the different Fermi wave vectors k_F, and also different critical phonon wave vectors q_c at valley $\pm K$. This provides an origin for two neighboring sudden jumps of CPD in Figures 7B–7D, since the two critical phonon wave vectors q_c from valley $\pm K$ are quite close to each other. This is in contrast to the case without layer potential difference, where there is a single sudden jump as shown in Figures 4 and 5.

Figures 7B–7D show the CPD of layer-*S*, layer-*A*, and cross-phonon-responses, respectively. The geometries of these responses are given by Figures 3A–3C, respectively. The contribution of each phonon mode is indicated by the color. When compared to the layer-*S*, CPD in Figures 4D and 7B shows enhanced magnitude near the critical point q_c as a result of nonzero *V*. Compared to the layer-*A* CPD in Figure 5D, the qualitative behaviors are changed in Figure 7C, even including the sign. This means that the CPD is sensitive to the details of band structure, and can be tuned by the layer potential difference *V*. Intriguingly, the CPD in the cross-channel is introduced as a result of inversion symmetry breaking. The behaviors of such cross-phonon-responses are provided in Figure 7D, where different phonon modes are studied. Basically, the qualitative behaviors are similar to the layer-*S* and layer-*A* CPD, and also they share the same order of magnitude. Therefore the occurrence of CPD in the cross-channel provides a fingerprint for the inversion symmetry breaking in bilayer system.

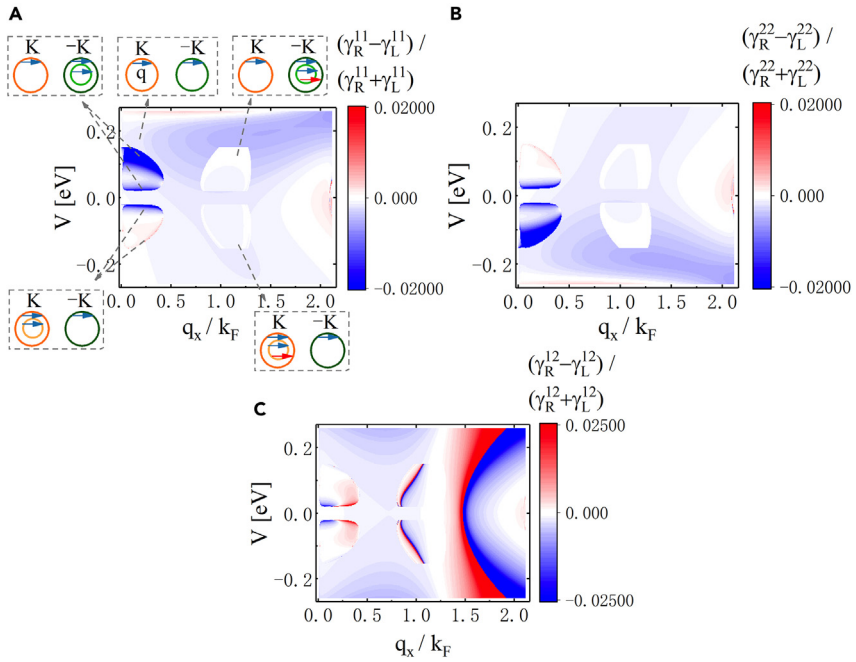

Figure 10. CPD of layer-1, layer-2, and interlayer responses versus phonon wave vector q_x and layer potential difference V

(A) CPD of layer-1 responses. Schematics of Fermi pockets and allowed electronic transitions induced by phonons are shown in the inset. The parameters are the same as those adopted in Figure 4.

(B) CPD of layer-2 responses.

(C) CPD of interlayer responses.

It is more intuitive to understand the role of V in the representation of individual layers, whose results are shown in Figure 8. Figures 8A and 8B plot the intralayer CPD within layer 1 and 2, respectively, whereas Figures 8C and 8D plot the interlayer CPD. The setups of Figures 8A–8C correspond to Figures 3D–3F, respectively. Compared to the case without layer potential difference V, we find that the CPD within layer 1 and 2 becomes unequal (see Figures 8A and 8B), which is a natural result of inversion symmetry breaking. Figures 8C and 8D show the same results, suggesting that the CPD of bilayer graphene is reciprocal. Moreover, the qualitative features of interlayer CPD are similar to those in Figures 6C and 6D. For example, they have the same discontinuous point $q_x = q_d$. However, the magnitude of interlayer CPD is enhanced by introducing V. Therefore the introduction of layer potential difference V provides a possible way to tune various types of CPD in bilayer graphene.

To demonstrate this, we further discuss the behaviors of CPD for different gate potentials. The results at fixed Fermi energy $E_F = 0.18$ eV are plotted in Figure 9. In Figure 9A, when q_x is small and by introducing V, the magnitude of layer-S CPD can be largely enhanced, up to about 0.01. Such enhancement is due to the occurrence of multiple Fermi pockets at valley K or -K, which are indicated in the insets. The allowed intraband electronic transitions induced by phonons are also labeled by arrows. The layer-S CPD shows symmetric behaviors by reversing the sign of V. Similar behaviors can also be seen in Figures 9B and 9C. Particularly, in Figure 9C, CPD for cross-phonon-response $(\Gamma_R^{SA} - \Gamma_L^{SA})/(\Gamma_R^{SA} + \Gamma_L^{SA})$ shows sign change for small value of q_x by tuning V. At $V = 0$, the CPD vanishes, which agrees with previous results without layer potential difference.

On the other hand, the results of CPD in the layer representation are plotted in Figure 10. The magnitude and sign of intralayer and interlayer CPD can be tuned versus phonon wave vector q_x and V. The behaviors of layer-1 and layer-2 CPD become asymmetric between V and $-V$, whereas the interlayer CPD is symmetric. Due to the existence of layer potential difference V, layer-1 and layer-2 CPDs are no longer equivalent; however, they become equivalent when the sign of V is also reversed. In Figure 10A, there are regions around $q_x/k_F \approx 1$ with vanishingly small CPD. The occurrence of these anomalous behaviors is due to additional contributions of CPD from interband electronic transitions with multiple Fermi pockets (see red arrows in the insets).

DISCUSSION AND CONCLUSION

To conclude, we have studied various types of CPD in bilayer graphene. We find that pseudo-gauge-type electron-phonon coupling, rather than scalar deformation potentials, is necessary to exhibit the CPD. When the system preserves the inversion symmetry, the layer-S and layer-A CPD are present, whereas the CPD in the cross-channel vanishes. The intralayer CPD from different layers is equal. The introduction of layer potential difference V breaks the inversion symmetry. This modifies the layer-S and layer-A CPD, and also induces the CPD in the cross-channel. In the layer representation, the intralayer CPD from different layers becomes unequal. This study provides opportunities to utilize the layer degree of freedom to control and tune the phonon dynamics in bilayer graphene.

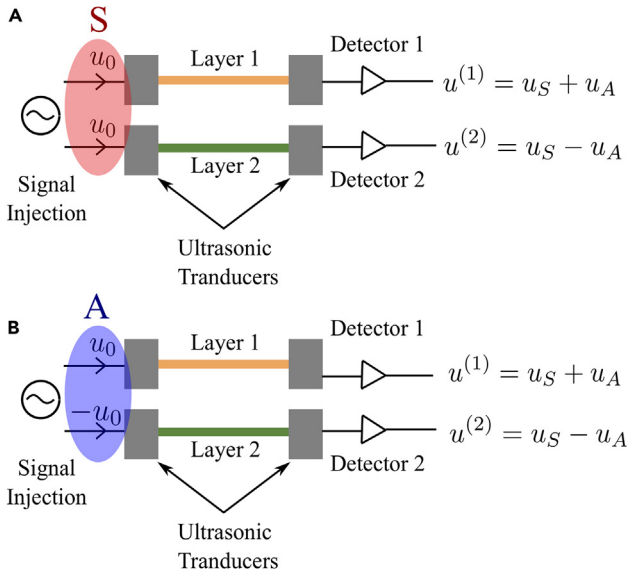

Figure 11. Schematics of the ultrasonic pulse-echo measurement on bilayer graphene

(A) With layer-*S* injection. Detection from different layers $u^{(1)}$ and $u^{(2)}$ can be decomposed into layer-*S* and layer-*A* components $u_{S/A}$.

(B) With layer-*A* injection.

Note that our treatment is at the harmonic level. Phonon anharmonicity, originating from three- or four-phonon interactions, enters the phonon equation of motion in a nonlinear manner and introduces the coupling between in-plane stretching and out-of-plane bending or flexural phonon modes.[42] As a result, phonon dispersion and phonon lifetime are modified.[43] However, small amounts of strain, due either to the pinning to the substrate or to the gate-induced electrostatic force, are enough to suppress the anharmonic effects.[44,45] Therefore, in our situation, anharmonic effects can be neglected.

The gate-tunable phonon dichroism effect can be experimentally detected by the ultrasonic pulse-echo technique.[46,47] The setup is shown schematically in Figure 11. In Figure 11A, layer-*S* waves are injected, and transmitted wave amplitudes from both layers are detected, i.e., $u^{(1)}$ and $u^{(2)}$. For a system with inversion symmetry breaking, $u^{(1)}$ and $u^{(2)}$ become unequal. In this case, $u^{(1)}$ and $u^{(2)}$ can be decomposed into layer-*S* and layer-*A* components, i.e., $u_{S/A}$, where the existence of u_A is a natural result of inversion symmetry breaking. u_S and u_A correspond to the response Γ^{SS} and Γ^{SA}, respectively. Therefore, the response Γ^{SA} in the cross-channel can be used as a signature of inversion symmetry breaking in bilayer system. Similarly, in Figure 11B, when layer-*A* waves are injected, the response Γ^{AS} can be extracted from experimental data as a fingerprint for inversion symmetry breaking. For an order-of-magnitude estimate, at $q_x/k_F = 0.233$ and $V = 0.13$ eV, the difference of the attenuation between the left- and right-handed circularly polarized waves read $2|\Gamma_E^{SS}|/\bar{v} \approx 1560/m$, where $\bar{v} = (v_r + v_t)/2$ is the average sound velocity. Similarly, for layer-*A* and cross-phonon-responses, $2|\Gamma_E^{AA}|/\bar{v} \approx 1480/m$ and $2|\Gamma_C^{SA} - \Gamma_I^{SA}|/\bar{v} \approx 1880/m$. Such differences are much larger than those of the Weyl semimetals[16] and monolayer transition metal dichalcogenides,[17] and should be observable in ultrasonic experiments. On the other hand, the CPD can also be detected by the Raman spectroscopy analysis of phonon polarization.[22] Such effect may find practical applications as acoustic circular polarizers, which induce circular polarization from linearly polarized acoustic waves.

Our studies are not restricted to bilayer graphene, but can be applied to other bilayer systems, such as bilayer transition metal dichalcogenides.[48,49] This can be even generalized to nonelectronic systems, for example, magnon-phonon coupled systems.[50] In addition to the layer degree of freedom, there are other degrees of freedom, such as the twist angle,[51,52] which may also be used to tune the phonon dynamics. This will be the subject of future work.

Limitations of the study

We neglect trigonal warping term in the model. Multi-dimensional mapping of the CPD with respect to the parameters layer potential difference V, phonon wave vector q_x, Fermi energy E_F, and magnetic exchange interaction M requires too much data to be plotted and is difficult to present.

STAR★METHODS

Detailed methods are provided in the online version of this paper and include the following:

- KEY RESOURCES TABLE
- RESOURCE AVAILABILITY

ACKNOWLEDGMENTS

We are grateful to Yurong Weng for many valuable discussions and comments. This work is supported by the National Natural Science Foundation of China (NSFC, grant nos. 11904062 and 12374175), the Starting Research Fund from Guangzhou University (grant no. RQ2020076), and Guangzhou Basic Research Program, jointly funded by Guangzhou University (grant no. 202201020186).

AUTHOR CONTRIBUTIONS

W.-Y.S. supervised the project, performed theoretical calculations, and prepared the figures and the manuscript.

DECLARATION OF INTERESTS

The authors declare no competing interests.

Received: September 28, 2023
Revised: January 30, 2024
Accepted: February 27, 2024
Published: March 4, 2024

REFERENCES

1. Xiao, D., Chang, M.-C., and Niu, Q. (2010). Berry phase effects on electronic properties. Rev. Mod. Phys. *82*, 1959–2007.
2. Cheng, B., Schumann, T., Wang, Y., Zhang, X., Barbalas, D., Stemmer, S., and Armitage, N.P. (2020). A Large Effective Phonon Magnetic Moment in a Dirac Semimetal. Nano Lett. *20*, 5991–5996.
3. Baydin, A., Hernandez, F.G.G., Rodriguez-Vega, M., Okazaki, A.K., Tay, F., Noe, G.T., Katayama, I., Takeda, J., Nojiri, H., Rappl, P.H.O., et al. (2022). Magnetic Control of Soft Chiral Phonons in PbTe. Phys. Rev. Lett. *128*, 075901.
4. Ren, Y., Xiao, C., Saparov, D., and Niu, Q. (2021). Phonon Magnetic Moment from Electronic Topological Magnetization. Phys. Rev. Lett. *127*, 186403.
5. Saparov, D., Xiong, B., Ren, Y., and Niu, Q. (2022). Lattice dynamics with molecular Berry curvature: Chiral optical phonons. Phys. Rev. B *105*, 064303.
6. Hernandez, F.G.G., Baydin, A., Chaudhary, S., Tay, F., Katayama, I., Takeda, J., Nojiri, H., Okazaki, A.K., Rappl, P.H.O., Abramof, E., et al. (2023). Observation of interplay between phonon chirality and electronic band topology. Sci. Adv. *9*, adj4074.
7. Zhang, X.-W., Ren, Y., Wang, C., Cao, T., and Xiao, D. (2023). Gate-Tunable Phonon Magnetic Moment in Bilayer Graphene. Phys. Rev. Lett. *130*, 226302.
8. Geilhufe, R.M., and Hergert, W. (2023). Electron magnetic moment of transient chiral phonons in $KTaO_3$. Phys. Rev. B *107*, L020406.
9. Luo, J., Lin, T., Zhang, J., Chen, X., Blackert, E.R., Xu, R., Yakobson, B.I., and Zhu, H. (2023). Large effective magnetic fields from chiral phonons in rare-earth halides. Science *382*, 698–702.
10. Barkeshli, M., Chung, S.B., and Qi, X.-L. (2012). Dissipationless phonon Hall viscosity. Phys. Rev. B *85*, 245107.
11. Hamada, M., and Murakami, S. (2020). Phonon rotoelectric effect. Phys. Rev. B *101*, 144306.
12. Nomura, T., Zhang, X.-X., Zherlitsyn, S., Wosnitza, J., Tokura, Y., Nagaosa, N., and Seki, S. (2019). Phonon Magnetochiral Effect. Phys. Rev. Lett. *122*, 145901.
13. Sengupta, S., Lhachemi, M.N.Y., and Garate, I. (2020). Phonon Magnetochiral Effect of Band-Geometric Origin in Weyl Semimetals. Phys. Rev. Lett. *125*, 146402.
14. Hu, L.-H., Yu, J., Garate, I., and Liu, C.-X. (2021). Phonon Helicity Induced by Electronic Berry Curvature in Dirac Materials. Phys. Rev. Lett. *127*, 125901.
15. Parlak, S., Ghosh, S., and Garate, I. (2023). Detection of phonon helicity in nonchiral crystals with Raman scattering. Phys. Rev. B *107*, 104308.
16. Liu, D., and Shi, J. (2017). Circular Phonon Dichroism in Weyl Semimetals. Phys. Rev. Lett. *119*, 075301.
17. Shan, W.-Y. (2022). Anomalous circular phonon dichroism in transition metal dichalcogenides. Phys. Rev. B *105*, L121302.
18. Shan, W.-Y. (2023). Nonreciprocal phonon dichroism induced by Fermi pocket anisotropy in two-dimensional Dirac materials. Phys. Rev. Res. *5*, L022038.
19. Shan, W.-Y. (2023). Phonon dichroism in proximitized graphene. Chin. Phys. B *32*, 106301.
20. Kossacki, P., Faugeras, C., Kühne, M., Orlita, M., Mahmood, A., Dujardin, E., Nair, R.R., Geim, A.K., and Potemski, M. (2012). Circular dichroism of magnetophonon resonance in doped graphene. Phys. Rev. B *86*, 205431.
21. Kumaravadivel, P., Greenaway, M.T., Perello, D., Berdyugin, A., Birkbeck, J., Wengraf, J., Liu, S., Edgar, J.H., Geim, A.K., Eaves, L., and Krishna Kumar, R. (2019). Strong magnetophonon oscillations in extra-large graphene. Nat. Commun. *10*, 3334.
22. Sonntag, J., Reichardt, S., Beschoten, B., and Stampfer, C. (2021). Electrical Control over Phonon Polarization in Strained Graphene. Nano Lett. *21*, 2898–2904.
23. Oostinga, J.B., Heersche, H.B., Liu, X., Morpurgo, A.F., and Vandersypen, L.M.K. (2008). Gate-induced insulating state in bilayer graphene devices. Nat. Mater. *7*, 151–157.
24. Xia, F., Farmer, D.B., Lin, Y.-M., and Avouris, P. (2010). Graphene Field-Effect Transistors with High On/Off Current Ratio and Large Transport Band Gap at Room Temperature. Nano Lett. *10*, 715–718.
25. Zhang, Y., Tang, T.-T., Girit, C., Hao, Z., Martin, M.C., Zettl, A., Crommie, M.F., Shen, Y.R., and Wang, F. (2009). Direct observation of a widely tunable bandgap in bilayer graphene. Nature *459*, 820–823.
26. Taychatanapat, T., and Jarillo-Herrero, P. (2010). Electronic Transport in Dual-Gated Bilayer Graphene at Large Displacement Fields. Phys. Rev. Lett. *105*, 166601.
27. Sui, M., Chen, G., Ma, L., Shan, W.-Y., Tian, D., Watanabe, K., Taniguchi, T., Jin, X., Yao, W., Xiao, D., and Zhang, Y. (2015). Gate-tunable topological valley transport in bilayer graphene. Nat. Phys. *11*, 1027–1031.
28. Shimazaki, Y., Yamamoto, M., Borzenets, I.V., Watanabe, K., Taniguchi, T., and Tarucha, S. (2015). Generation and detection of pure valley current by electrically induced Berry curvature in bilayer graphene. Nat. Phys. *11*, 1032–1036.

29. Gao, A., Liu, Y.-F., Hu, C., Qiu, J.-X., Tzschaschel, C., Ghosh, B., Ho, S.-C., Bérubé, D., Chen, R., Sun, H., et al. (2021). Layer Hall effect in a 2D topological axion antiferromagnet. Nature *595*, 521–525.
30. Chen, R., Sun, H.-P., Gu, M., Hua, C.-B., Liu, Q., Lu, H.-Z., and Xie, X.C. (2024). Layer Hall effect induced by hidden Berry curvature in antiferromagnetic insulators. Natl. Sci. Rev. *11*, nwac140.
31. Qiao, Z., Tse, W.-K., Jiang, H., Yao, Y., and Niu, Q. (2011). Two-Dimensional Topological Insulator State and Topological Phase Transition in Bilayer Graphene. Phys. Rev. Lett. *107*, 256801.
32. Tse, W.-K., Qiao, Z., Yao, Y., MacDonald, A.H., and Niu, Q. (2011). Quantum anomalous Hall effect in single-layer and bilayer graphene. Phys. Rev. B *83*, 155447.
33. Qiao, Z., Li, X., Tse, W.-K., Jiang, H., Yao, Y., and Niu, Q. (2013). Topological phases in gated bilayer graphene: Effects of Rashba spin-orbit coupling and exchange field. Phys. Rev. B *87*, 125405.
34. Mendes, J.B.S., Alves Santos, O., Meireles, L.M., Lacerda, R.G., Vilela-Leão, L.H., Machado, F.L.A., Rodríguez-Suárez, R.L., Azevedo, A., and Rezende, S.M. (2015). Spin-Current to Charge-Current Conversion and Magnetoresistance in a Hybrid Structure of Graphene and Yttrium Iron Garnet. Phys. Rev. Lett. *115*, 226601.
35. Wang, Z., Tang, C., Sachs, R., Barlas, Y., and Shi, J. (2015). Proximity-Induced Ferromagnetism in Graphene Revealed by the Anomalous Hall Effect. Phys. Rev. Lett. *114*, 016603.
36. Mariani, E., Pearce, A.J., and von Oppen, F. (2012). Fictitious gauge fields in bilayer graphene. Phys. Rev. B *86*, 165448.
37. Suzuura, H., and Ando, T. (2002). Phonons and electron-phonon scattering in carbon nanotubes. Phys. Rev. B *65*, 235412.
38. Verberck, B., Partoens, B., Peeters, F.M., and Trauzettel, B. (2012). Strain-induced band gaps in bilayer graphene. Phys. Rev. B *85*, 125403.
39. Vozmediano, M.A.H., Katsnelson, M.I., and Guinea, F. (2010). Gauge fields in graphene. Phys. Rep. *496*, 109–148.
40. Shan, W.-Y. (2020). Impact of novel electron-phonon coupling mechanisms on valley physics in two-dimensional materials. Phys. Rev. B *102*, 241301.
41. Landau, L.D., and Lifshitz, E.M. (1986). Theory of Elasticity, 3rd ed. (Pergamon Press), pp. 101–103.
42. Michel, K.H., Costamagna, S., and Peeters, F.M. (2015). Theory of anharmonic phonons in two-dimensional crystals. Phys. Rev. B *91*, 134302.
43. Yan, X., Wang, B., Hai, Y., Kripalani, D.R., Ke, Q., and Cai, Y. (2022). Phonon anharmonicity and thermal conductivity of two-dimensional van der Waals materials: A review. Sci. China Phys. Mech. Astron. *65*, 117004.
44. Roldán, R., Fasolino, A., Zakharchenko, K.V., and Katsnelson, M.I. (2011). Suppression of anharmonicities in crystalline membranes by external strain. Phys. Rev. B *83*, 174104.
45. Bonini, N., Garg, J., and Marzari, N. (2012). Magnetic Control of Soft Chiral Phonons in PbTe. Nano Lett. *12*, 2673–2678.
46. Truell, R., Elbaum, C., and Chick, B.B. (1969). Ultrasonic Methods in Solid State Physics (Academic Press), pp. 53–70.
47. Lüthi, B. (2004). Physical Acoustics in the Solid State (Springer), pp. 7–16.
48. Cheiwchanchamnangij, T., and Lambrecht, W.R.L. (2012). Quasiparticle band structure calculation of monolayer, bilayer, and bulk MoS_2. Phys. Rev. B *85*, 205302.
49. Lui, C.H., Ye, Z., Ji, C., Chiu, K.-C., Chou, C.-T., Andersen, T.I., Means-Shively, C., Anderson, H., Wu, J.-M., Kidd, T., et al. (2015). Observation of interlayer phonon modes in van der Waals heterostructures. Phys. Rev. B *91*, 165403.
50. Lyons, T.P., Puebla, J., Yamamoto, K., Deacon, R.S., Hwang, Y., Ishibashi, K., Maekawa, S., and Otani, Y. (2023). Acoustically driven magnon-phonon coupling in a layered antiferromagnet. Preprint at arXiv. https://doi.org/10.48550/arXiv.2303.08305.
51. Lopes dos Santos, J.M.B., Peres, N.M.R., and Castro Neto, A.H. (2012). Continuum model of the twisted graphene bilayer. Phys. Rev. B *86*, 155449.
52. Liu, X., Peng, R., Sun, Z., and Liu, J. (2022). Moiré Phonons in Magic-Angle Twisted Bilayer Graphene. Nano Lett. *22*, 7791–7797.

STAR★METHODS

KEY RESOURCES TABLE

REAGENT or RESOURCE	SOURCE	IDENTIFIER
Software and algorithms		
MATLAB 2019b	Mathworks	https://www.mathworks.com/products/matlab.html
Origin pro 2019	Origin lab corporation	https://www.orginlab.com

RESOURCE AVAILABILITY

Lead contact

Further information and requests for resources and reagents should be directed to and will be fulfilled by the lead contact, Wen-Yu Shan (wyshan@gzhu.edu.cn).

Materials availability

This study did not generate new unique reagents.

Data and code availability

- All data reported in this paper will be shared by the lead contact upon request.
- This paper does not report original code.
- Any additional information requested to reanalyze the data reported in this paper is available from the lead contact upon request.

EXPERIMENTAL MODEL AND STUDY PARTICIPANT DETAILS

This study does not use experimental models typical in the life sciences.

METHOD DETAILS

Phonon dynamics

In the presence of electron-phonon coupling, phonon equation of motion follows

$$\omega^2 U(\boldsymbol{q}) = \hbar^2 \Phi(\boldsymbol{q}) U(\boldsymbol{q}) - \frac{\hbar^2}{\rho_0 V} T(\boldsymbol{q}), \quad \text{(Equation 12)}$$

where the spinor $U(\boldsymbol{q}) = [u_x^{(1)}(\boldsymbol{q}), u_y^{(1)}(\boldsymbol{q}), u_x^{(2)}(\boldsymbol{q}), u_y^{(2)}(\boldsymbol{q})]^T$ and the average force $T(\boldsymbol{q}) = [\langle \widehat{T}_x^{(1)}(\boldsymbol{q})\rangle, \langle \widehat{T}_y^{(1)}(\boldsymbol{q})\rangle, \langle \widehat{T}_x^{(2)}(\boldsymbol{q})\rangle, \langle \widehat{T}_y^{(2)}(\boldsymbol{q})\rangle]^T$ are defined in the layer representation. $\langle \cdots \rangle$ is the expectation value evaluated in the electron subsystem in the presence of electron-phonon coupling. $\Phi(\boldsymbol{q})$ is the dynamical matrix and V is the area.

Based on the linear response theory, we have $\hbar T(\boldsymbol{q})/\rho_0 V = -\chi(\boldsymbol{q},\omega) U(\boldsymbol{q})$, where the response matrix

$$\chi(\boldsymbol{q},\omega) = \left[\chi_{ij}^{lk}\right] = \begin{bmatrix} \chi_{xx}^{11} & \chi_{xy}^{11} & \chi_{xx}^{12} & \chi_{xy}^{12} \\ \chi_{yx}^{11} & \chi_{yy}^{11} & \chi_{yx}^{12} & \chi_{yy}^{12} \\ \chi_{xx}^{21} & \chi_{xy}^{21} & \chi_{xx}^{22} & \chi_{xy}^{22} \\ \chi_{yx}^{21} & \chi_{yy}^{21} & \chi_{yx}^{22} & \chi_{yy}^{22} \end{bmatrix}. \quad \text{(Equation 13)}$$

Each of the retarded response functions $\chi_{ij}^{lk}(\boldsymbol{q},\omega)$ can be decomposed into valley-resolved tensors

$$\chi_{ij}^{lk}(\boldsymbol{q},\omega) = \sum_{\eta=\pm 1} \chi_{ij}^{lk,\eta}(\boldsymbol{q},\omega) = \sum_{\eta=\pm 1} \sum_{n,m} \int \frac{\hbar d^2 \boldsymbol{k}}{\rho_0 (2\pi)^2} F_{nm}^{\eta}(\omega,\boldsymbol{k},\boldsymbol{q}) \left[G_{ij}^{lk,\eta}(\omega,\boldsymbol{k},\boldsymbol{q})\right]_{mn}, \quad \text{(Equation 14)}$$

where $i,j = \{x,y\}$, $l,k = \{1,2\}$ and m,n are band indices of electronic Hamiltonian $H_e(\boldsymbol{k})$. The dynamical factor

$$F^{\eta}_{nm}(\omega,\boldsymbol{k},\boldsymbol{q}) = \frac{f_{\eta,m,k} - f_{\eta,n,k'}}{\omega+i\delta+E_{\eta,m,k} - E_{\eta,n,k'}} \quad \text{(Equation 15)}$$

and geometric factor

$$\left[G^{lk,\eta}_{ij}(\omega,\boldsymbol{k},\boldsymbol{q})\right]_{mn} = \langle\psi_{\eta,m,k}|\widehat{T}^{\eta}_{i,l}(\boldsymbol{q})|\psi_{\eta,n,k'}\rangle\langle\psi_{\eta,n,k'}|\widehat{T}^{\eta}_{j,k}(-\boldsymbol{q})|\psi_{\eta,m,k}\rangle, \quad \text{(Equation 16)}$$

with $\boldsymbol{k}' = \boldsymbol{k} - \boldsymbol{q}$. $E_{\eta,m/n,k}$ and $|\psi_{\eta,m/n,k}\rangle$ are eigen-dispersion and wave functions of $H_e(\boldsymbol{k})$, respectively. $f_{\eta,m,k}$ ($f_{\eta,n,k'}$) is the Fermi distribution function. For bilayer graphene, a single band intersects the Fermi level at each valley, thus we can set $m = n$ hereafter.

The phonon absorption corresponds to the anti-Hermitian part of $\chi(\boldsymbol{q},\omega)$ matrix, that is, $-2i\omega\gamma(\boldsymbol{q},\omega)$. As a result, the Hermitian matrix $\gamma(\boldsymbol{q},\omega)$ is given by

$$\gamma(\boldsymbol{q},\omega) = \frac{i}{4\omega}\{\chi(\boldsymbol{q},\omega) - [\chi(\boldsymbol{q},\omega)]^{+}\}, \quad \text{(Equation 17)}$$

whose matrix form follows

$$\gamma(\boldsymbol{q},\omega) = \begin{bmatrix} \gamma^{11}_{xx} & \gamma^{11}_{xy} & \gamma^{12}_{xx} & \gamma^{12}_{xy} \\ \gamma^{11}_{yx} & \gamma^{11}_{yy} & \gamma^{12}_{yx} & \gamma^{12}_{yy} \\ \gamma^{21}_{xx} & \gamma^{21}_{xy} & \gamma^{22}_{xx} & \gamma^{22}_{xy} \\ \gamma^{21}_{yx} & \gamma^{21}_{yy} & \gamma^{22}_{yx} & \gamma^{22}_{yy} \end{bmatrix}. \quad \text{(Equation 18)}$$

The elements γ^{lk}_{ij} are

$$\gamma^{lk}_{ij}(\boldsymbol{q},\omega) = -\frac{\hbar}{2\rho_0\omega}\sum_{\eta=\pm1}\sum_{n}\int\frac{d^2\boldsymbol{k}}{(2\pi)^2}\mathrm{Im}\left[F^{\eta}_{nn}(\omega,\boldsymbol{k},\boldsymbol{q})\right]\left[G^{lk,\eta}_{ij}(\omega,\boldsymbol{k},\boldsymbol{q})\right]_{nn}, \quad \text{(Equation 19)}$$

where $i,j = \{x,y\}$ and $l,k = 1,2$. For acoustic phonons, phonon energy ω is much smaller than the Fermi energy E_F, and in the low-temperature limit,

$$\mathrm{Im}\left[F^{\eta}_{nn}(\omega,\boldsymbol{k},\boldsymbol{q})\right] \approx -\pi\omega\delta(E_{\eta,n,k} - E_F)\delta(\omega + E_{\eta,n,k} - E_{\eta,n,k'}). \quad \text{(Equation 20)}$$

Substituting this relation into above equation, each of $\gamma^{lk}_{ij}(\boldsymbol{q},\omega)$ can be obtained by integrating out two delta functions. For convenience, γ matrix can be rewritten as

$$\gamma(\boldsymbol{q},\omega) = \begin{bmatrix} \gamma^{11}(\boldsymbol{q},\omega) & \gamma^{12}(\boldsymbol{q},\omega) \\ \gamma^{21}(\boldsymbol{q},\omega) & \gamma^{22}(\boldsymbol{q},\omega) \end{bmatrix}, \quad \text{(Equation 21)}$$

where these 2 by 2 blocks take the form

$$\gamma^{ll}(\boldsymbol{q},\omega) = \begin{bmatrix} \gamma^{ll}_{D} + \gamma^{ll}_{\overline{D}} & \gamma^{ll}_{\overline{E}} + i\gamma^{ll}_{E} \\ \gamma^{ll}_{\overline{E}} - i\gamma^{ll}_{E} & \gamma^{ll}_{D} - \gamma^{ll}_{\overline{D}} \end{bmatrix}, ll = 1,2,$$
$$\gamma^{12}(\boldsymbol{q},\omega) = \begin{bmatrix} \gamma^{12}_{B} + i\gamma^{12}_{\overline{B}} & \gamma^{12}_{\overline{C}} + i\gamma^{12}_{C} \\ \gamma^{12}_{I} + i\gamma^{12}_{I} & \gamma^{12}_{J} + i\gamma^{12}_{\overline{J}} \end{bmatrix}. \quad \text{(Equation 22)}$$

All of the absorption coefficients $\gamma^{ll}_{D/\overline{D}}$, $\gamma^{ll}_{E/\overline{E}}$, $\gamma^{12}_{B/\overline{B}}$, $\gamma^{12}_{C/\overline{C}}$, $\gamma^{12}_{I/\overline{I}}$ and $\gamma^{12}_{J/\overline{J}}$ are real. Numerically, we find that $\gamma^{12}_{\overline{B}} = \gamma^{12}_{\overline{J}} = \gamma^{12}_{\overline{C}} = \gamma^{12}_{\overline{I}} = 0$. Other coefficients can be derived based on the definitions

$$\begin{aligned}
\gamma_D^{ll} &= \frac{1}{2}\left(\gamma_{xx}^{ll} + \gamma_{yy}^{ll}\right) \\
&= -\frac{\hbar}{4\rho_0\omega}\sum_{\eta,n}\int\frac{d^2\boldsymbol{k}}{(2\pi)^2}\mathrm{Im}\left[F_{nn}^{\eta}\right]\left[G_{xx}^{ll,\eta}+G_{yy}^{ll,\eta}\right]_{nn}, \\
\gamma_{\overline{D}}^{ll} &= \frac{1}{2}\left(\gamma_{xx}^{ll} - \gamma_{yy}^{ll}\right) \\
&= -\frac{\hbar}{4\rho_0\omega}\sum_{\eta,n}\int\frac{d^2\boldsymbol{k}}{(2\pi)^2}\mathrm{Im}\left[F_{nn}^{\eta}\right]\left[G_{xx}^{ll,\eta} - G_{yy}^{ll,\eta}\right]_{nn}, \\
\gamma_E^{ll} &= \mathrm{Im}\left[\gamma_{xy}^{ll}\right] = -\frac{\hbar}{2\rho_0\omega}\sum_{\eta,n}\int\frac{d^2\boldsymbol{k}}{(2\pi)^2}\mathrm{Im}\left[F_{nn}^{\eta}\right]\mathrm{Im}\left[G_{xy}^{ll,\eta}\right]_{nn}, \\
\gamma_{\overline{E}}^{ll} &= \mathrm{Re}\left[\gamma_{xy}^{ll}\right] = -\frac{\hbar}{2\rho_0\omega}\sum_{\eta,n}\int\frac{d^2\boldsymbol{k}}{(2\pi)^2}\mathrm{Im}\left[F_{nn}^{\eta}\right]\mathrm{Re}\left[G_{xy}^{ll,\eta}\right]_{nn}
\end{aligned} \tag{Equation 23}$$

and

$$\begin{aligned}
\gamma_B^{12} &= \gamma_{xx}^{12} = -\frac{\hbar}{2\rho_0\omega}\sum_{\eta,n}\int\frac{d^2\boldsymbol{k}}{(2\pi)^2}\mathrm{Im}\left[F_{nn}^{\eta}\right]\left[G_{xx}^{12,\eta}\right]_{nn}, \\
\gamma_C^{12} &= -i\gamma_{xy}^{12} = \frac{i\hbar}{2\rho_0\omega}\sum_{\eta,n}\int\frac{d^2\boldsymbol{k}}{(2\pi)^2}\mathrm{Im}\left[F_{nn}^{\eta}\right]\left[G_{xy}^{12,\eta}\right]_{nn}, \\
\gamma_I^{12} &= -i\gamma_{yx}^{12} = \frac{i\hbar}{2\rho_0\omega}\sum_{\eta,n}\int\frac{d^2\boldsymbol{k}}{(2\pi)^2}\mathrm{Im}\left[F_{nn}^{\eta}\right]\left[G_{yx}^{12,\eta}\right]_{nn}, \\
\gamma_J^{12} &= \gamma_{yy}^{12} = -\frac{\hbar}{2\rho_0\omega}\sum_{\eta,n}\int\frac{d^2\boldsymbol{k}}{(2\pi)^2}\mathrm{Im}\left[F_{nn}^{\eta}\right]\left[G_{yy}^{12,\eta}\right]_{nn}.
\end{aligned} \tag{Equation 24}$$

On the other hand, phonon absorption can be studied in the layer-symmetric (S) and antisymmetric (A) representation. In this representation, the deformations and forces are related to those in the layer representation by

$$\begin{aligned}
U(\boldsymbol{q}) &= P\overline{U}(\boldsymbol{q}) = P\begin{bmatrix} u_{x,S} \\ u_{y,S} \\ u_{x,A} \\ u_{y,A} \end{bmatrix}, \\
T(\boldsymbol{q}) &= \frac{1}{2}P\overline{T}(\boldsymbol{q}) = \frac{1}{2}P\begin{bmatrix} \langle\widehat{T}_{x,S}(\boldsymbol{q})\rangle \\ \langle\widehat{T}_{y,S}(\boldsymbol{q})\rangle \\ \langle\widehat{T}_{x,A}(\boldsymbol{q})\rangle \\ \langle\widehat{T}_{y,A}(\boldsymbol{q})\rangle \end{bmatrix},
\end{aligned} \tag{Equation 25}$$

where the transformation matrix follows

$$P = \begin{bmatrix} 1 & 0 & -1 & 0 \\ 0 & 1 & 0 & -1 \\ 1 & 0 & 1 & 0 \\ 0 & 1 & 0 & 1 \end{bmatrix}. \tag{Equation 26}$$

In the new representation, the response matrix $X(\boldsymbol{q},\omega)$ is introduced by the definition $\hbar\overline{T}(\boldsymbol{q})/\rho_0 V = -X(\boldsymbol{q},\omega)\overline{U}(\boldsymbol{q})$. As a result, we find a relation between the response matrix $X(\boldsymbol{q},\omega)$ and $\chi(\boldsymbol{q},\omega)$:

$$X(\boldsymbol{q},\omega) = 2P^{-1}\chi(\boldsymbol{q},\omega)P. \tag{Equation 27}$$

Similarly, phonon absorption corresponds to the anti-Hermitian part of $X(\boldsymbol{q},\omega)$ matrix, that is, $-2i\omega\Gamma(\boldsymbol{q},\omega)$. This gives rise to the Hermitian matrix

$$\Gamma(\boldsymbol{q},\omega) = \frac{i}{4\omega}\{X(\boldsymbol{q},\omega) - [X(\boldsymbol{q},\omega)]^{+}\}, \quad \text{(Equation 28)}$$

with the matrix form

$$\Gamma(\boldsymbol{q},\omega) = \begin{bmatrix} \Gamma_{xx}^{SS} & \Gamma_{xy}^{SS} & \Gamma_{xx}^{SA} & \Gamma_{xy}^{SA} \\ \Gamma_{yx}^{SS} & \Gamma_{yy}^{SS} & \Gamma_{yx}^{SA} & \Gamma_{yy}^{SA} \\ \Gamma_{xx}^{AS} & \Gamma_{xy}^{AS} & \Gamma_{xx}^{AA} & \Gamma_{xy}^{AA} \\ \Gamma_{yx}^{AS} & \Gamma_{yy}^{AS} & \Gamma_{yx}^{AA} & \Gamma_{yy}^{AA} \end{bmatrix}. \quad \text{(Equation 29)}$$

The elements $\Gamma_{ij}^{\alpha\beta}$ are

$$\Gamma_{ij}^{\alpha\beta}(\boldsymbol{q},\omega) = -\frac{\hbar}{2\rho_0\omega}\sum_{\eta=\pm1}\sum_{n} \int \frac{d^2\boldsymbol{k}}{(2\pi)^2}\mathrm{Im}\left[F_{nn}^{\eta}(\omega,\boldsymbol{k},\boldsymbol{q})\right]\left[G_{ij}^{\alpha\beta,\eta}(\omega,\boldsymbol{k},\boldsymbol{q})\right]_{nn}, \quad \text{(Equation 30)}$$

where $i,j = \{x,y\}$ and $\alpha,\beta = S,A$. Similar to Equation 27, there is a relation between $\Gamma(\boldsymbol{q},\omega)$ and $\gamma(\boldsymbol{q},\omega)$:

$$\Gamma(\boldsymbol{q},\omega) = 2P^{-1}\gamma(\boldsymbol{q},\omega)P. \quad \text{(Equation 31)}$$

$\Gamma(\boldsymbol{q},\omega)$ matrix can also be written in block form

$$\Gamma(\boldsymbol{q},\omega) = \begin{bmatrix} \Gamma^{SS}(\boldsymbol{q},\omega) & \Gamma^{SA}(\boldsymbol{q},\omega) \\ \Gamma^{AS}(\boldsymbol{q},\omega) & \Gamma^{AA}(\boldsymbol{q},\omega) \end{bmatrix}, \quad \text{(Equation 32)}$$

where

$$\Gamma^{\alpha\alpha}(\boldsymbol{q},\omega) = \begin{bmatrix} \Gamma_{D}^{\alpha\alpha} + \Gamma_{\overline{D}}^{\alpha\alpha} & \Gamma_{\overline{E}}^{\alpha\alpha} + i\Gamma_{E}^{\alpha\alpha} \\ \Gamma_{\overline{E}}^{\alpha\alpha} - i\Gamma_{E}^{\alpha\alpha} & \Gamma_{D}^{\alpha\alpha} - \Gamma_{\overline{D}}^{\alpha\alpha} \end{bmatrix}, \alpha = S,A,$$
$$\Gamma^{SA}(\boldsymbol{q},\omega) = \begin{bmatrix} \Gamma_{B}^{SA} + i\Gamma_{\overline{B}}^{SA} & \Gamma_{\overline{C}}^{SA} + i\Gamma_{C}^{SA} \\ \Gamma_{\overline{J}}^{SA} + i\Gamma_{J}^{SA} & \Gamma_{J}^{SA} + i\Gamma_{\overline{J}}^{SA} \end{bmatrix}. \quad \text{(Equation 33)}$$

All of the absorption coefficients $\gamma_{D/\overline{D}}^{\alpha\alpha}$, $\gamma_{E/\overline{E}}^{\alpha\alpha}$, $\gamma_{B/\overline{B}}^{SA}$, $\gamma_{C/\overline{C}}^{SA}$, $\gamma_{I/\overline{I}}^{SA}$ and $\gamma_{J/\overline{J}}^{SA}$ are real. Numerically, we find that $\Gamma_{\overline{B}}^{SA} = \Gamma_{\overline{J}}^{SA} = \Gamma_{\overline{C}}^{SA} = \Gamma_{\overline{I}}^{SA} = 0$.

QUANTIFICATION AND STATISTICAL ANALYSIS

There is no statistical analysis or quantification in this paper.

ADDITIONAL RESOURCES

There are no additional resources needed to be declared in this manuscript, additional requests for this can be made by contacting the lead contact.